AN ALGORITHM FOR FORECASTING MOUNTAIN WAVE RELATED TURBULENCE IN THE STRATOSPHERE

Julio T. Bacmeister

Naval Research Laboratory, Washington D.C., 20375

Paul A. Newman

NASA Goddard Space Flight Center, Greenbelt, MD, 20771

Bruce Gary

NASA Jet Propulsion Laboratory, Pasadena, CA, 91109

Roland Chan

NASA Ames Research Center, Moffet Field, CA, 94035

August 1992

Abstract.

A Global mountain wave parameterization for prediction of wave related displacements and turbulence is described. The parameterization is used with input from NMC analyses of wind and temperature to examine small-scale disturbances encountered by the NASA high-altitude ER-2 during the Second Airborne Arctic Stratosphere Experiment (AASE II). The magnitude and location of observed large wave events are well reproduced. A strong correlation is suggested between patches of moderate turbulence encountered by the ER-2 and locations where breaking mountain waves are predicted by the parameterization. These facts suggest that useful forecasts of global mountain wave activity, including wave related CAT, can be made quickly and inexpensively using our mountain wave parameterization with input from current numerical forecast models.

1. Introduction

The connection of stratospheric turbulence to mountain wave activity has long been recognized c.f. Ehernberger (1987). However, the complexities of mountain flows have prevented the development of useful forecasting tools for use on a global scale. Part of the difficulty lies in the com-

plicated nature of topographic forcing. Real topography possesses a rich spatial spectrum which like that of many natural phenomena obeys a power-law [Mark and Aronson, 1984]. However, the topographic spectrum is not in general isotropic [Steyn and Ayotte, 1985]. In other words there are directional differences (anisotropy) in the magnitude and scale of topographic variance. This anisotropy is clearly evident in the fact that much of Earth's topography is organized into relatively long, narrow ridges. The orientation of these ridges is an important variable in determining the wave response of the atmosphere to topography.

This study will describe improvements to a mountain wave parameterization scheme introduced in Bacmeister [1992] which allow reliable forecasts of mountain wave amplitudes in the upper- troposphere and lower stratosphere to be made based on standard meteorological products from operational forecasting models such as the NMC T126 MRF model. The basis for these mountain wave forecasts is a global, computer-generated list of prominent topographic ridges containing parameters such as lat, lon, orientation, approximate altitude and approximate width for each ridge. The algorithm used to construct this data set is described in Section 2a of this study. Mountain wave quantities are calculated using the WKB approximation with wave amplitudes limited to saturation values as done in earlier parameterizations e.g. Macfarlane [1987]. This calculation is described in detail in Section 2b. In Section 3 predicted wave amplitudes and turbulence intensities are compared with observations of wind and temperature collected by NASA ER-2 s during AASE II.

2. Description of Mountain Wave Parameterization

The theoretical basis for the parameterization used in this study is the same as that in [Bacmeister, 1992]. However, significant improvements have been made to the description of topographic forcing used in the present parameterization. The study of [Bacmeister, 1992] examined the effects of topographic anisotropy (ridginess) on estimates of mountain wave drag in the middle atmosphere. The topographic forcing in this study was based on a box-by-box analysis of topographic features with scales of between 50 and 100km in a gridbox of size $250x250km^2$. Only one ridge was assumed to exist within each gridbox and no attempt

was made to segregate features by width or to identify features with scales smaller than 50km. While this approach may have been adequate for an initial assessment of anisotropic effects and comparison with other coarse-grained gravity wave parameterizations, a more detailed model was needed for operational forecasting of flight conditions in the stratosphere and for subsequent comparison with airplane observations.

The 'ridge-finding' algorithm described below differs from that in [Bacmeister, 1992] in several respects.

a. "Ridge-Finding" Algorithm

Topographic data was obtained from a global data set compiled by NCAR containing mean elevations within 5'x5' rectangles. This data was used to produce a global list of ridges containing the location, orientation, and approximate height and width of each ridge. The analysis of the topographic data consisted of 8 basic steps

1- interpolation to grid with equal spacing (in km) in zonal and meridional directions.

2- band pass filtering.

3- normalization by local mean variance.

4- elimination of variance below chosen threshhold value.

5- comparison at each point with idealized ridglets at 36 different orientations.

6- selection of 'good' matches.

7- estimate of actual terrain elevation.

8- reconstruction of topography.

Each step is described in detail below.

Step 1)

Interpolation is performed to remove distortions arising from the Earth's sphericity. This is accomplished

in a crude way by performing the calculation along 10° latitude strips in which the raw 5'x5' topographic data was interpolated onto a grid with equal spacing in km in both directions. Thus, in the case of a 10° strip centered at 60° the raw 4320x120 data array is interpolated onto a 2160x120 array before further processing. In general, the raw 4320x120 strips at latitude θ are interpolated to $INT(sin(\theta) \bullet 4320)$x120 arrays, where $INT(z)$ refers to the largest integer smaller than z. The strip centers are spaced 5° apart in latitude.

Step 2)

Band pass filtering is accomplished by subtracting the results of two different square boxcar filters applied to the interpolated topographic data. This step controls the scale of feature identified by the subsequent steps in the algorithm. The set of ridges used in this study was determined from four different band-passed filtered topographic data sets. The high-pass, L_{hp}, and low-pass, L_{lp}, limits for each of these are listed in Table 1. The result of this operation will be referred to as the topographic deviation and denoted - dev_{topo}.

Step 3)

Next, a running mean of the absolute value of the band-pass filtered topography is determined. This is done with a square boxcar filter of size $10L_{hp}$. The band-pass filtered topography, Dev_{topo}, from step 2 is then divided by this quantity at each point to give a 'normalized' topographic deviation at each point.

Step 4)

The normalized topographic deviation from step 3 is examined at each point. Values greater than or equal to than a threshhold value of +1.25 are replaced with 1.00 and values less than this threshhold are replaced with 0. The result of this operation will be referred to as the 'skeleton' topography and denoted $Skel_{topo}$. The exact value of the threshhold does not appear to have major impact on the rest of processing as long as it is between 1.00 and 2.00. If a much higher value is chosen the algorithm becomes too discriminating, choosing only the highest isolated peaks in any region. If a threshhold value lower than 1.00 is chosen, the separation between major and minor terrain features is lost. Subsequent processing is more time consuming and appears to be less accurate since spurious 'ridges' may be

introduced connecting major and minor features. The selection of the 'best' threshhold was accomplished by trial and error.

Step 5)

The skeleton topography, $Skel_{topo}$, is then compared with 36 idealized 'ridglets' $R(x_i, y_j, x_0, y_0, n; L_{hp})_{n=1,..,36}$ at each point (x_0, y_0) in the $Skel_{topo}$ array. The ridglet functions R are defined to have a value of 1.00 within an L_{hp} x $3L_{hp}$ rectangle about a central point (x_0, y_0) and a value of 0 for all (x_i, y_j) outside of the rectangle. 36 different trial orientations differing by 5° are used at each point. The comparison of the idealized ridglets with $Skel_{topo}$ at (x_0, y_0) is accomplished by calculating the sum

$$f(x_0, y_0, n) = \frac{\sum\sum R'(x_i, y_j, x_0, y_0, n_0) Skel'_{topo}(x_i, y_j)}{\sqrt{\sum\sum [R'(x_i, y_j, x_0, y_0, n_0)]^2}} \qquad (1)$$

for each orientation n, where $()'$ refers to the deviation of the quantity from a running mean over a $3L_{hp}$ x $3L_{hp}$ square.

Step 6)

The sums $f(x_0, y_0, n)$ in step 5 can vary from -1 to +1. Unfortunately, the ridge-functions R are not orthogonal. However, the value of the sum f increases as the similarity between the underlying topography and the trial ridge-function increases. Thus, in order to determine the orientation of the underlying terrain features at each point (x_0, y_0), the 36 sums $f(x_0, y_0, n)$ are searched for the orientation index n_0 associated with the highest value of f. Next, all points (x_0, y_0) in the topographic array are searched for negative values of $f(x_0, y_0, n_0)$. These negative values are discarded. This eliminates 'trenches' or canyons from consideration. Finally, each L_{hp} x L_{hp} square in the topography array is examined separately for the highest value of f contained within and only this value is kept. This is done to eliminate as much redundancy as possible in the list of ridges before further use.

Step 7)

Once a list of the location and orientation of possible ridges is obtained an estimate of actual elevation changes across each ridge is made. The estimate is obtained from

the sum:

$$a(x_0, y_0, n_0) = \frac{\sum R'(x_i, y_j, x_0, y_0, n_0) Dev_{topo}(x_i, y_j)}{\sqrt{\sum [R'(x_i, y_j, x_0, y_0, n_0)]^2}} \quad (2)$$

The quantity a is simply the projection of the topographic deviation from step 2 onto the ridge-function $R'(x_i, y_j, x_0, y_0, n_0)$. The relationship of a to the actual valley-to-peak ridge height depends on details of the terrain shape. However, for a wide variety of real and idealized ridge profiles a is between 1/3 and 1/4 of the actual ridge height.

Step 8)

At this point in the processing each choice of band-pass parameters L_{hp} and L_{lp} is associated with a list of topographic features. Each feature or 'ridgelet' is assigned a position (x_k, y_k), an orientation n_k, a 'ridginess' index $f(x_k, y_k, n_k)$ and a ridge-height parameter $a(x_k, y_k, n_k)$ where the subscript k denotes the k-th ridge in the list. The full list of ridges contains redundancy since the functions R at different points may overlap. The basic strategy for dealing with redundancy in the list of ridges is as follows. First, the list is ordered by the size of the height parameter a with the highest ridge coming first. Next, the ridges are laid one-by-one, starting with the highest, onto a flat surface at the appropriate location (x_k, y_k). Each ridglet is represented simply by the expression

$$ridglet_k(x_i, y_j) = 4a(x_k, y_k, n_k) R(x_i, y_j, x_k, y_k, n_k; L_{hp,k}) \quad (3)$$

If some of the area covered by the latest ridge is already covered by previous ridges, the newest ridge does not add elevation to that area. A 'weight' is determined from the fraction of the new ridge which is not covered by previous, higher ridges. If 25% of the new ridge is exposed and 75% is covered by higher ridges then the new ridge is assigned a weight of 0.25 and so on. This is repeated until all ridglets in the list have been placed on the surface. At the end of this procedure, redundancies within a given list of ridges have been accounted for by the fact that in any pair of overlapping ridges at least one of the ridges will have weight less than 1.0

Clearly, redundancies within lists of ridglets of the same width should be accounted for. However, the situation across lists corresponding to different ridge widths is not clear. A single point in the topographic array may be covered by several ridglets of different widths. In the following study we have assumed that such redundancy reflects true topographic structure and may thus be ignored.

A straightforward approach involving FFT's of topographic elevation data was not used to construct the ridge data set for several reasons. First, a large number of modes is required to obtain the same accuracy in the estimate of dominant ridge orientation. Thus, either a large subarray of topography must be used or, small subarrays of topography must be interpolated onto a finer grid. Using a large subdomain both increases the possibility of mulitiple ridges in a given subarray as well as reducing the accuracy with which individual features can be localized in physical space. If small subarrays of topographic data are used aritificial edges at the subarray boundaries must be dealt with in some fashion. Second, in either case FFT's cannot accurately represent the orientation features with relatively small aspect ratios such as 3:1. However, such features may still exhibit "ridge-like" behavior in a stratified flow Hines (1988).

Results of the step-by-step processing described above applied to the topography of Alaska and Northwestern Canada are shown in Fig. 1. The results shown are for band pass parameters $L_{hp} = 50km$ and $L_{lp} = 128km$. The final result for this region including features from all 4 width ranges is shown in Fig. 1d. Major topographic features such as the Alaska Range and the Canadian Rockies are clearly evident and accurately reproduced in the final reconstruction. Secondary features such as topography on the Aleutian Islands and Queen Charlotte Islands (132W, 53N) are also captured. In Section 3 it will be shown that such "secondary" topography, in this case the Laurentian Mountains and Notre Dame Mountains of Southern Quebec, can produce noticeable turbulence at Stratospheric altitudes.

Fig. 1

b. Estimate of Mountain Wave Activity

The list of topographic ridges developed in Sec.2a allows global mountain wave activity to be estimated on a ridge-

by-ridge basis. Background wind and stratification near each ridge are determined from NMC T126 MRF forecast and/or NMC CAC analysis fields. In the calculations discussed here we simply use data from the NMC gridpoint nearest to each ridge center (x_k, y_k). The estimate of wave amplitudes is made essentially as in b92. First, the profile of the wind component perpendicular to the "k-th" ridge $U_{\perp;k}(z)$ is calculated using the ridge orientation n_k found in Sec. 2a. We assume that the waves launched by each ridge are purely 2-dimensional with wave crests parallel to the generating ridge at all levels. We also assume the waves are hydrostatic so that wave activity is generally localized over the forcing topography. The average momentum flux profile over any ridge can be approximated in terms of the wave vertical displacement profile:

$$\phi_k(z) \sim \alpha\rho(z)N_k(z)U_{\perp;k}(z)\frac{\delta_k(z)^2}{L} \tag{4}$$

where $\delta_k(z)$ is the profile of wave-induced vertical displacement above the "k-th" ridge, $N_k(z)$ the profile of stratification frequency above the ridge, and $\rho(z)$ is the background atmospheric density profile which we assume is simply proportional to pressure. The parameter α is a dimensionless factor which depends on ridge shape and L is horizontal length representing the extent of the wave disturbance. As will be seen below, these last two parameters drop out in the calculation of the wave displacement profile.

We assume further that wave momentum flux remains constant with height until wave breaking occurs. This will be the case for hydrostatic waves in a slowly varying (with altitude) atmosphere. Our criterion for wave breaking is based on simulations of 2-dimensional flow over topography which suggest that wave amplitudes do not exceed the local saturation limit given by

$$\delta_{sat;k}(z) \equiv U_{\perp;k}(z)/N_k(z) \tag{5}$$

Using (4) and (5) we can construct an approximate wave displacement profile as follows: Given $\delta_k(z)$ at some analysis level we use (4) to make a provisional guess of the displacement at the next level $\delta_k^*(z + \Delta z)$; then, if the provisional $\delta_k^*(z + \Delta z)$ exceeds the saturation limit (5) it is arbitrarily reduced to the saturation limit before pro-

ceeding to the next level, i. e.;

$$\delta_k^*(z+\Delta z) = \delta_k(z)\sqrt{\frac{\rho(z)N_k(z)U_{\perp;k}(z)}{\rho(z+\Delta z)N_k(z+\Delta z)U_{\perp;k}(z+\Delta z)}} \quad (6)$$

$$\delta_k(z+\Delta z) = MIN\left[\delta_k^*(z+\Delta z), \delta_{sat;k}(z+\Delta z)\right] \quad (7)$$

In order to complete the determination of $\delta_k(z)$ the wave displacement at the surface must be known. For the lower boundary we use;

$$\delta_k(z_0) = MIN\left[4a_k, U_{\perp;k}(z_0)/N_k(z_0)\right] \quad (8)$$

where a_k is the ridge height parameter defined in (2). The lowest level z_0 used over a particular ridge depends on the estimated height of a particular ridge above sea-level. The total height of ridge 'k' is estimated as $H_k + 4a_k$ where H_k is the mean elevation in a 2.5° x 2.5° box containing the center of ridge 'k'. We attempt to use wind and stratification near mountain top level in each calculation, thus, the closest analysis/forecast level to mountain-top level is used as z_0. Possible refinements of this algorithm which include the possibility of turning by strong jets will be discussed in Sec. 3.

Once profiles of wave induced vertical displacements $\delta_k(z)$ over each ridge are obtained estimates of other wave quantities can be made. Wave induced potential temperature perturbations are estimated according to;

$$\theta_k'(z) = \delta_k(z)\partial_z\Theta_{NMC} \quad (9)$$

where Θ_{NMC} is the background potential temperature from the NMC analysis/forecast.

c. Estimate of Wave-Induced Turbulence

The mechanisms which actually limit wave amplitudes to the saturation limit (5) are still controversial. However, it is likely that when wave amplitudes approach the saturation limit at least some of the wave energy will go into localized convective instabilities. This assertion is well supported by both two-dimensional numerical simulations

and linear wave theories. Thus, in the model described here wave-induced turbulence is forecast whenever saturation is invoked to limit wave amplitudes in (6) and (7). Furthermore, we assume *ad hoc* that the intensity of the turbulence in a layer is proportional to the amount of momentum flux lost by the wave within that layer, i.e.;

$$KE_{Turbulence}(z + \Delta z/2) \propto \phi_k(z) - \phi_k(z + \Delta z) \qquad (10)$$

where $\phi_k(z)$ is the momentum flux defined in (4) and $KE_{Turbulence}$ is a representative magnitude of the Kinetic Energy in small scale ($\leq 1000m$) motions in a given layer.

At this stage values must be assigned to the parameters α and L in (4). We assume $\alpha \approx 1.5$ based on two-dimensional, numerical simulations as suggested in Pierrehumbert [1987]. This value is based on experiments over smooth symmetric obstacles, so its general applicability is rightly questioned. However, quantitative estimates for α in flow over realistic obstacles are not available. We assume the length scale L is of secondary importance in estimating turbulence intensities in breaking waves. This is because the production of turbulence along a section of a breaking wave will depend on the *total* flux of wave momentum flux from below rather than on instantaneous momentum flux densities. The total momentum flux in a hydrostatic wave is independent of the obstacle width. For definiteness we assign L a value of 50km.

NOTE FOR AIR FORCE FORECASTERS:

"Turbulence Potential" maps produced by the model sent to you in May simply show $\phi_k(z) - \phi_k(z + \Delta z)$ above each ridge (calculated in module GET_WVTURB.PRO). However, to be on the safe side the model looks at the momentum flux change in the layer above a given level AND in the layer below. The larger value of the 2 is chosen as the "Turbulence Potential" for a given level. So, for example, to produce the 70mb map from the NMC forecast, the model looks at the momentum flux change over each ridge between 70mb and 50mb, and then at the change between 100mb and 70mb. The larger value for each ridge is then returned. Also, although I can't prove it with the data I have looked at upto now, I think low Richardson Number based on $U_{\perp;k}(z)$ and $N_k(z)$ could increase the chance of

strong turbulence in a breaking wave (see Sec. 4a). So, I included the option of a Richardson Number enhancement in the module GET_WVTURB.PRO. This just multiplies the original "Turbulence Potential" by a factor $100/Ri$ whenever the ridge perpendicular Richardson Number, Ri, goes below 100. This is very crude but at least highlights breaking waves for which the environmental Richardson Number is low.

3. Model Verification

Three clear examples of encounters with mountain waves in the stratosphere occurred during the AASEII campaign. Two of these encounters were accompanied by pilot reports of moderate turbulence. For the purpose of model verification, global mountain wave predictions will be made below using NMC 18-level analyses of wind and temperature for each day on which a mountain wave was encountered by the ER-2. The predictions of the model along the ER-2 flight track will be compared with wind and and potential temperature observations collected by on-board instruments during each of the wave encounters. The wind data used is from the Meteorological Measurement System (MMS) which provides 3-components of wind, as well as temperature and pressure at a frequency of 1Hz [Chan et al., 1989]. Temperature and potential temperature profiles are derived from Microwave Temperature Profiler (MTP) data. The MTP provides a temperature profile composed of 15 independent measurements extending approximately 3km above and below the aircraft [Gary, 1989]. A complete profile is obtained once every 7 seconds. This can be integrated vertically after suitable averaging to obtain pressure and potential temperature profiles. The individual potential temperature profiles can be joined along the flight track to obtain a cross-section illustrating the vertical displacements of potential temperature surfaces along the flight path.

a. 10/14/91 Mountain wave observation

Fig. 2

On 10/14/91 the NASA ER-2 was ferried back to its home base at Moffet Field CA from the AASEII mission site at Fairbanks AL. Fig. 2a shows the ER-2 flight track from Fairbanks to Moffet Field as well as a map of tur-

AK

bulence potential for 10/14/91. The turbulence potential map consists of gray shaded symbols representing ridges in the list described in Sec. 2a. The color of each symbol denotes the possible intensity of wave induced turbulence over each ridge at 70mb. This is determined by calculating the differences; $\phi(100mb) - \phi(70mb)$, and $\phi(70mb) - \phi(50mb)$, where ϕ is the wave momentum flux in $(ms^{-1})^2(kgm^{-3})$ defined in Eq.(4). The larger of the two differences is then scaled from 0 to 1 $(ms^{-1})^2(kgm^{-3})$. This produces a map showing the largest predicted amount of momentum flux deposited by mountain waves in the layers above and below 70mb. As discussed in Sec. 2b momentum flux deposition is assumed to be proportional to the local turbulent scale kinetic energy. The size of each symbol shows the approximate size of the ridge element generating each predicted wave disturbance. For hydrostatic waves generated by ridges the wave energy is confined near the forcing, thus the map gives an idea of where turbulence may expected.

On this flight the ER-2 flew through regions where relatively high turbulence intensities were predicted. In fact, the pilot reported moderate turbulence and rapid temperature fluctuations over the coastal ranges of southern Alaska. The MTP potential temperature cross-section for 10/14/91 (Fig. 2b) confirms the existence of waves. Large vertical displacements, ~ 500 to $800m$ were recorded between 68000 and 71000 seconds Universal Time (UT) as the plane crossed over the Alaska, Wrangell, and Chugach Ranges in Southeastern Alaska. The vertical displacements predicted by the global mountain wave model along the flight track are also shown in Fig. 2b. The displacements shown represent the prediction of the mountain wave parameterization at aircraft altitude at each point along the track. The zero line has been moved to 22.5 km for display purposes. It should be kept in mind that the parameterization predicts only peak wave amplitude. No phase information is included. Thus, the sign of displacements is not predicted. In Fig. 2b all predicted displacements are arbitrarily assigned a positive sign. Nevertheless, Fig. 2b shows that there is rough agreement between predictions and observations in both the amplitude and location of large vertical displacements. The parameterization somewhat overpredicts the amplitude of the largest displacements. However, the observed displacements may depend sensitively on the exact position (to within 10km) of the

plane relative to each mountain wave. The current parameterization cannot resolve detailed structure within each wave. Therefore, exact agreement between predictions and observations cannot be expected.

To obtain an objective measure of the turbulence intensities encountered by the ER-2 rapid fluctuations in MMS vertical wind data were examined. Fig. 2c shows Variance in 5 sec vertical velocity fluctuations averaged over a 100sec window, i.e.;

$$\left\langle [w(t+5sec) - w(t)]^2 \right\rangle_{100sec}$$

for the 10/14/91 ferry flight. Variance far in excess of background levels was observed between 68000 and 71000 UT as the ER-2 flew through the mountain waves over SE Alaska. Fig. 2c also shows the predicted drop in wave momentum flux near aircraft altitude along the flight track;

$$\Delta\phi \equiv \phi(z_{i-}) - \phi(z_{i+})$$

where z_{i-} is the analysis level immediately below flight level and z_{i+} is the level immediately above. This differs slightly from the definition of the "turbulence potential" for Fig. 2a in that only the layer actually containing the aircraft is considered. Units of $\Delta\phi$ are also $(ms^{-1})^2(kgm^{-3})$. For display purposes, the zero line for $\Delta\phi$ in Fig. 2c has been moved to 2 on the y-axis The close agreement in peak amplitudes of wind variance in $(ms^{-1})^2$ and $\Delta\phi$ is a fortuitous consequence of our choices for α and L in (4) and of the air density near 70mb. It should not be expected to hold at other pressure levels. However, the close agreement between the location of the predicted "turbulence" and the location of the large values in vertical wind variance is meaningful and suggests that the turbulence encountered on this flight is indeed the result of breaking, large-amplitude mountain waves.

b. 1/6/92 Mountain wave observation

Fig. 3

On 1/6/92 the ER-2 flew NE from the AASE II mission base at Bangor ME across the southern tip of Greenland and back along the same track. Fig. 3a shows the ER-2 flight track and turbulence potential map for 1/6/92.

No potential for turbulence is predicted along the ER-2 track, although maps of predicted wave displacements (not shown) have 500m to 1000m displacements over S. Greenland. Pilot reports for this flight, list no turbulence or "chop". However, pressure altitude traces for this flight show a brief period of rapid but smooth ascent and descent over the tip of Greenland. This description is consistent with a large but non-turbulent mountain wave near the southern tip of Greenland as predicted by the parameterization.

The MTP cross-section for this flight, in Fig. 3b, shows moderate wave activity between 57000 and 62000 UT as the ER-2 flew near Greenland. A large displacement, about 800m, occurs at around 58000 UT and again at 61000 UT, immediately above the southern tip of Greenland on both the outbound and inbound legs of the flight. The predicted displacements for this day, in Fig. 3b, also show large values at this location. The amplitude of the predicted displacement is roughly correct. However, the predicted displacements occupy a smaller portion of the flight track than observed.

Fig. 3c shows the the 5-second, vertical wind variance for 1/6/92. Despite the absence of reported turbulence on this flight in Fig. 3c, shows weak but significant enhancement of vertical wind variability between 57000 and 62000 UT. The origin of this enhanced variability is unclear. It appears to coincide with "waviness" in the MTP section and may represent an enhancement in background variability over rough terrain [Nastrom and Fritts, 1992] or an enhancement due to the nearness of the polar vortex edge [McIntyre, 1989]. In any case we feel it is unlikely that the increase in small-scale variability near Greenland on this day was directly due to the breakdown of large amplitude mountain waves. The lack of significant wave induced turbulence at flight level despite the prediction of large wave displacements near Greenland is a consequence of strong on-ridge ($\sim$ westerly) wind speeds ($\sim 40ms^{-1}$) in this region. From Eq.(5) this implies saturation amplitude of nearly 2.0km for mountain waves assuming $N \approx 2.0 \times 10^{-2}s^{-1}$ near ER-2 altitudes.

c. 3/18/92 Mountain wave observation

Fig. 4

On 3/18/92 the ER-2 flew north from Bangor ME to Baffin Island and back. On the climb out of Bangor moderate turbulence was reported by the Pilot as the plane flew over the St. Lawrence River in SE Quebec. Fig. 4a shows the ER-2 flight track and turbulence potential map for 3/18/92. The map of turbulence potential shows relatively high values occurring on both sides of the St. Lawrence River, coinciding well the location of the reported turbulence.

The MTP section for this flight, in Fig. 4b, shows evidence of $\sim 300m$ to $500m$ vertical displacements between 48000 and 49000 UT during the climb out of Bangor and suggestions of another weak disturbance around 51000 UT. There appears to be rough agreement between predicted and observed displacements during climb out of Bangor. On descent back into Bangor there are also suggestions of vertical displacements around 73000 UT, however, the rapid descent of the plane makes these hard to distinguish in Fig. 4b. Displacements $\sim 500m$ are also predicted at 51000 and 71000 UT. At 51000 UT there is some suggestion of a vertically coherent perturbation in the MTP section. However, its amplitude is far below the predicted value. At 71000 UT, when the plane flew over the same topographic feature on the inbound leg of the mission, there is no readily discernible perturbation in the MTP section.

The topographic features responsible for the overpredicted displacements at 51000 and 71000 appear to be Monts Otish (52° N, 70° W, alt. $\sim 1000m$) as well as several other hills in South Central Quebec, all with altitudes of 900m to 1000m. For isolated, narrow features such as these, the assumptions of high anisotropy "ridginess" and hydrostatic balance may both fail. Thus, the algorithm described in Eqs.(4)-(8) may no longer be a valid approximate description of wave behavior. Both, nonhydrostatic effects and low "ridginess" will lead to horizontal dipsersion of wave energy. This will tend to lower wave amplitudes immediately above the forcing topography to values below those predicted by the model. On the other hand, the feature responsible for the waves encountered over the St. Lawrence River appear to be the Laurentian and Notre Dame mountains. These are somewhat broader and longer topographic features than the isolated hills described earlier. So that the assumptions made in Eqs.(4)-(8) about wave behavior are more closely satisfied.

Fig 4c shows observed 5-sec variability in vertical wind and predicted $\Delta\phi$ for 3/18/92. There is large $\Delta\phi$ predicted near aircraft altitude between 48000 and 50000 UT and again around 73000 UT as the ER-2 flew over the St. Lawrence River. The periods of large predicted $\Delta\phi$ correspond closely to periods of observed high variability in vertical wind, which suggests that the turbulence encountered at these locations is due to the breakdown of mountain waves forced by the Laurentian and Notre Dame mountains. As was the case for the 10/14/91 flight there is also rough agreement between the peak amplitudes of the variance in $(ms^{-1})^2$ and that of $\Delta\phi$ in $(ms^{-1})^2(kgm^{-3})$. Although it is premature to draw conclusions from two examples, these cases suggest a coincidental but possibly useful proportionality between $\Delta\phi$ and 5-second vertical wind variance close to 70mb level with a proportionality constant close to 1 $(kg^{-1}m^3)$.

The 3/18/92 mountain wave encounter is noteworthy because it suggests that even relatively minor topographic features, such as the Laurentian and Notre Dame mountains, may create significant turbulence in the lower stratosphere. This fact has implications for climate modelling as well as for turbulence forecasting. Parameterizations of mountain wave effects currently used in global forecasting and climate models use gridbox averages of topographic variance to estimate wave forcing. Even at the highest resolutions currently employed ($\sim 1^\circ \times 1^\circ$) this averaging will underestimate the potential of secondary features such as the Laurentian or Notre Dame ranges to exert signinficant drag on the atmosphere.

4. Possible improvements to model

The mountain wave parameterization described above relies on a simplified description of mountain wave behavior to predict wave ampiltudes above individual topographic features. An *ad hoc* assumption is made concerning the production of turbulence by breaking mountain waves. To some degree such simplifications are unavoidable in constructing a global mountain wave parameterization using inputs from current numerical forecasting models. However, we feel improvements can be made in certain aspects of the parameterization, in particular to the estimate of turbulence production by wave breaking.

a. Production of turbulence.

Fig. 5

The parameterization currently assumes a simple linear relationship between the momentum flux deposition in a layer, $\Delta\phi$, and turbulence intensity. This ignores possible interactions between the wave and the background wind. It is likely that waves breaking in a strongly sheared flow will produce stronger turbulence than those breaking in a uniform wind. Strong shears are generally thought to be rare in the stratosphere. However, it appears that planetary waves in the stratosphere can occasionally create relatively strong vertical gradients in on-ridge winds over individual ridges, as is illustrated in Fig 5. Fig. 5 shows NMC analyses of geopotential height for 1/16/92 over eastern Asia at 200,100, and 50 mb. The geostrophic wind in this situation weakened and changed direction considerably between 100 and 50mb, due to the presence of what appears to be a synoptic wave with amplitude increasing as a function of height. Thus, on-ridge winds decreased sharply with altitude between 100mb and 50mb for ridges in Korea and Japan. This drop in on-ridge wind speeds is reflected in the high turbulence potential due to wave breaking predicted at 70mb for these regions (Fig. 5d). Breaking mountain waves in this situation may have had enhanced levels of turbulence as a result of large shear in the background flow. Preliminary estimates of such an enhancement can be made with high-resolution, two-dimensional, numerical models such as those employed in studies of downslope windstorms [Peltier and Clark, 1979; Durran, 1986; and Bacmeister and Pierrehumbert, 1988].

b. Downstream Advection of Turbulence.

Several incidences of light to moderate "chop" over ocean were reported by ER-2 pilots during AASEII. Several of these occurred 100 to 500km downwind of areas where strong turbulence due to breaking mountain waves was forecast by the parameterization. It is possible that advection of turbulent kinetic energy away from breaking waves is an important source of turbulence away from mountainous terrain. Estimates of decay rates for turbulence in stratified flow are available (refs). These can be combined with turbulence production estimates from nonlinear simulations to give quantitative predictions for the downwind

extent and intensity of turbulent layers due produced by breaking mountain waves.

c. Nonhydrostatic Dispersion.

The parameterization currently assumes hydrostatic behavior for all mountain waves. However, Nonhydrostatic effects may become important for the narrowest set of ridges currently used (width $\sim 25km$) in regions with high wind. When hydrostatic balance is no longer satisfied, mountain wave energy begins to disperse downstream of the generating obstacle as the wave propagates vertically. This causes wave amplitudes to grow more slowly with height than they would for a hydrostatic wave. However, nonhydrostatic wave perturbations also expand progressively further downstream of the forcing obstacle with altitude. Thus, although nonhydrostatic waves may be weakened their effects may be felt siginificantly further downstream of the forcing obstacle than those of hydrostatic waves. In some cases high-winds can completely trap or "turn" vertically propagating waves at some level, creating the familiar lee-wave trains often observed downwind of narrow ridges. These trains of waves are primarily tropospheric phenomena. However, they usually signify that some fraction of the mountain wave spectrum from an obstacle can not propagate past strong tropospheric winds and will thus not contribute to stratospheric wave motion. Simple corrections for nonhydrostatic effects can be derived theoretically and are easily implemented in the existing parameterization.

References

Bacmeister, J. T.,Mountain wave drag in the stratosphere and mesosphere inferred from observed winds and a simple mountain wave parameterization scheme. (to appear *J. Atmos. Sci.*, 49)

Bacmeister, J. T. and R. T. Pierrehumbert, On high drag states of nonlinear, stratified flow over an obstacle. *J. Atmos. Sci.*, 45, 63-80, 1988

Chan, K. R., S. G. Scott, T. P. Bui, S. W. Bowen, and J. Day 1987: Temperature and horizontal wind measurements on the ER-2 aircraft during the 1987 Airborne Antarctic Ozone Experiment. *J. Geophys. Res.*,

94, 11573-11588, 1987.

Durran, D. R., Another look at downslope windstorms. Part I: On the development of analogs to supercritical flow in an infinitely deep continuously stratified fluid. *J. Atmos. Sci., 43,* 2527-2543, 1986.

Ehernberger, L. J., High Altitude Turbulence for Supersonic Cruise Vehicles. NASA Technical Memorandum 88285, May 1987.

Gary, B. L., Observational results using the microwave temperature profiler during the Airborne Antarctic Ozone Experiment. *J. Geophys. Res., 94,* 11223-11231, 1989.

Macfarlane, N. A., The effect of orographically excited gravity wave drag on the general circulation of the lower stratosphere and troposphere. *J. Atmos. Sci.*, 44, 1775-1800, 1987.

Mark, D. M., and P. B. Aaronson, Scale-dependent fractal dimension of topographic surfaces: An empirical investigation with application to geomorphology and computer mapping. *Math. Geol.*, 16, 671-683.

McIntyre, M. E., On the Antarctic ozone hole, *J. Atmos. Terr. Phys.*, 51, 29-43, 1989.

Nastrom, G. D., and D. C. Fritts 1992: Sources of mesoscale variability of gravity waves. Part I: Topographic excitation. *J. Atmos. Sci.*, 49, 101-110.

Peltier, W. R. and T. Clark, The evolution and stability of finite amplitude mountain waves. Part II: Surface drag and severe downslope windstorms. *J. Atmos. Sci.*, 36, 1498-1529, 1979.

Pierrehumbert, R. T., An essay on the parameterization of gravity wave drag. *ECMWF seminar/workshop report: Observation, theory and modelling of orographic effects*, 1, 251-282.

Steyn, D. G., and K. W. Ayotte, Application of two-dimensional terrain height spectra to mesoscale modeling. *J. Atmos. Sci.*, 42, 2884-2887, 1984

Julio T. Bacmeister, Code 4141, Naval Research Laboratory, Washington, DC, 20375, ph. (202) 767-2821.

Paul A. Newman, Code 916, NASA/GSFC, Greenbelt, MD 20771.

FIGURE CAPTIONS

Fig. 1. Processing of topography in Alaska and NW Canada. a) Original 5'x5' topography. "Lighting" is accomplished by subtracting elevation of a given point in the topography array from elevation of nearest neighbor to the northwest. This elevation change is then shaded with a linear gray scale where black represents -500m and white represents +500m . b) "Skeleton" topography. c) Best fit ridglets for widths $\sim 55km$. Ridgelets have been gray shaded according to height parameter a_k. d) Full reconstruction of topography using 4 sets of ridgelets. Shading is the same as in panel a.

Fig. 2. a) Map of turbulence potential and ER-2 flight track on 10/14/91. b) Potential Temperature as a function of time and height observed from the ER-2 on 10/14/91. Potential temperature Contours are drawn every 10K. Thin line superimposed on contours shows ER-2 flight track. Curve starting at 22.5km shows vertical displacements forecast at ER-2 altitude along flight track. A bias of 22.5km was added to displacements for display purposes. c) Lower curve; Variance in 5 sec vertical velocity fluctuations averaged over 100sec, i.e. $\langle [w(t+5sec) - w(t)]^2 \rangle_{100sec}$ as function of time on 10/14/91. Upper curve shows $\Delta\phi$ forecast along ER-2 flight track.

Fig. 3 As in Fig. 2 except for 1/6/92

Fig. 4 As in Fig. 2 except for 3/18/92

Fig. 5 (a) NMC analyses of geopotential height at 100mb (heavy solid lines), 50mb (dashed lines) over eastern Asia on 1/16/92. A synoptic scale wave with amplitude increasing as a function of altitude results in weak, almost northerly flow over Korea and Japan at 50mb. This produces a strong, negative, vertical gradient in on-ridge wind speed between 100mb and 50mb for several ridges in this region. A map of turbulence potential at 70mb due to breaking mountain waves is shown in (d). High turbulence potential is predicted for ridges under the stratospheric north-northwesterlies associated with the short planetary wave.

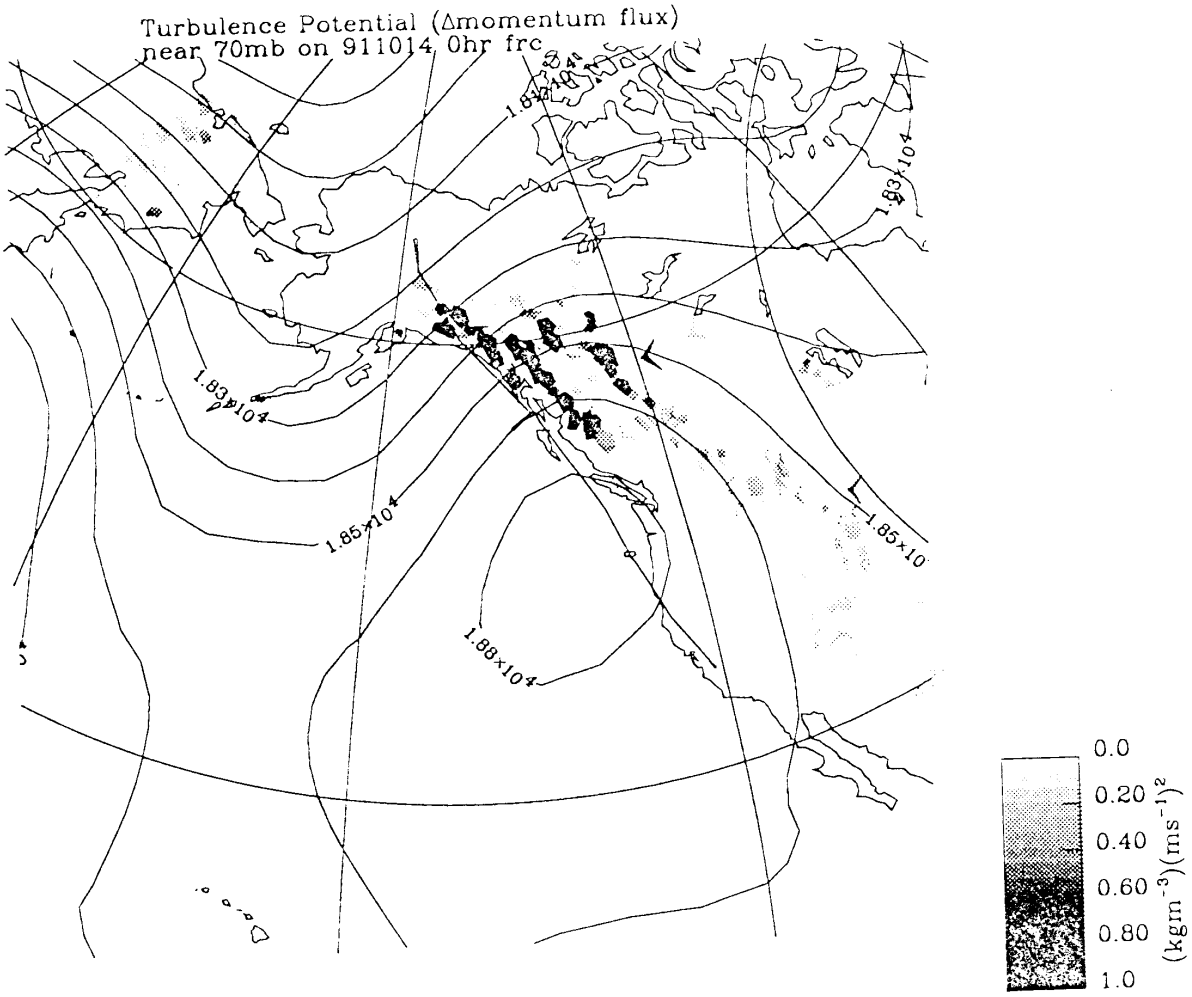
Turbulence Potential (Δmomentum flux)
near 70mb on 911014 0hr frc
1.83×10⁴
1.85×10⁴
1.88×10⁴
0.0
0.20
0.40
0.60
0.80
1.0
(kgm⁻³)(ms⁻¹)²

Fig. 2a

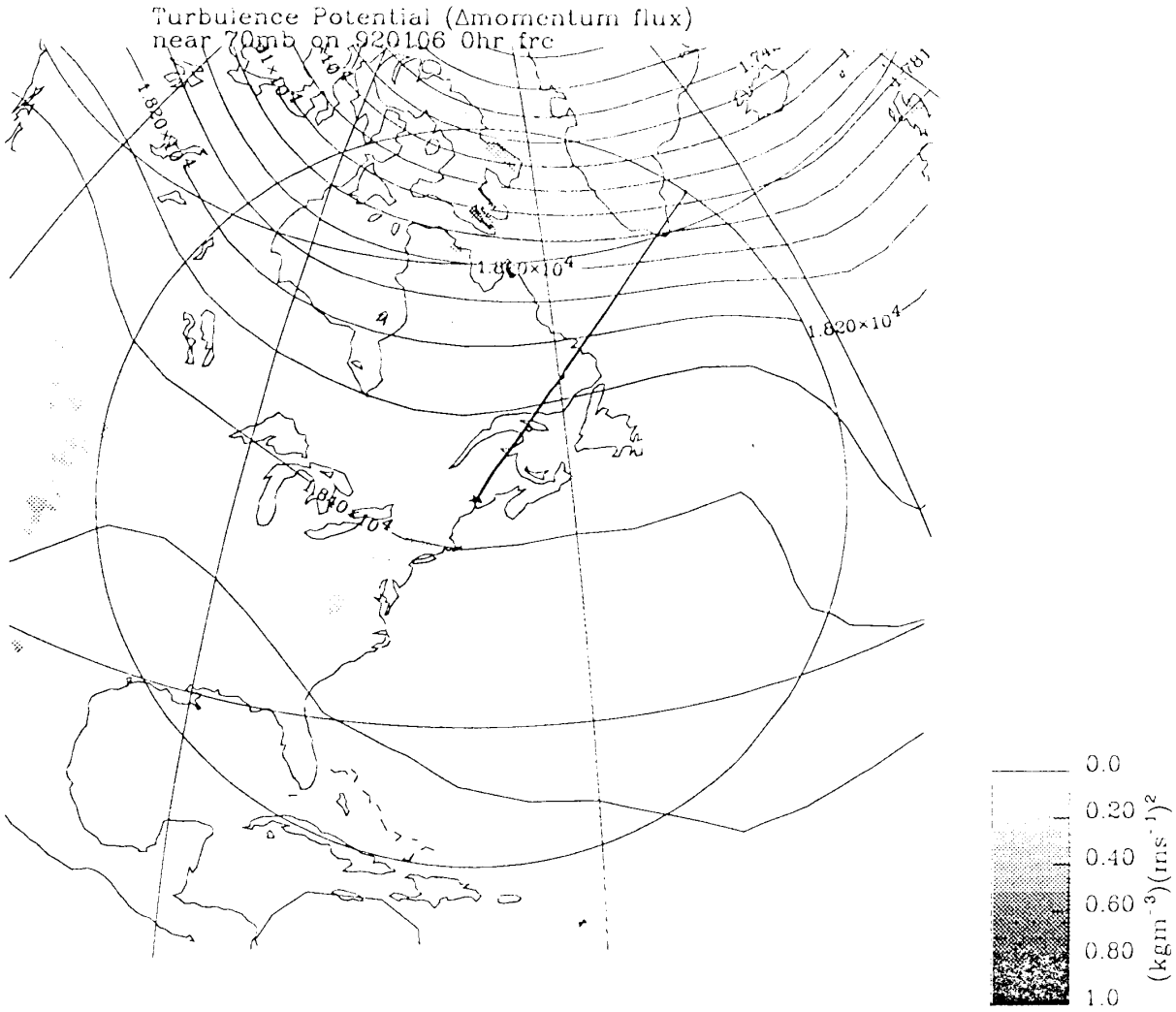
Turbulence Potential (Δmomentum flux)
near 70mb on 920106 0hr frc
1.820×10^4
0.0
0.20
0.40
0.60
0.80
1.0
(kgm^-3)(ms^-1)^2

Fig 3a

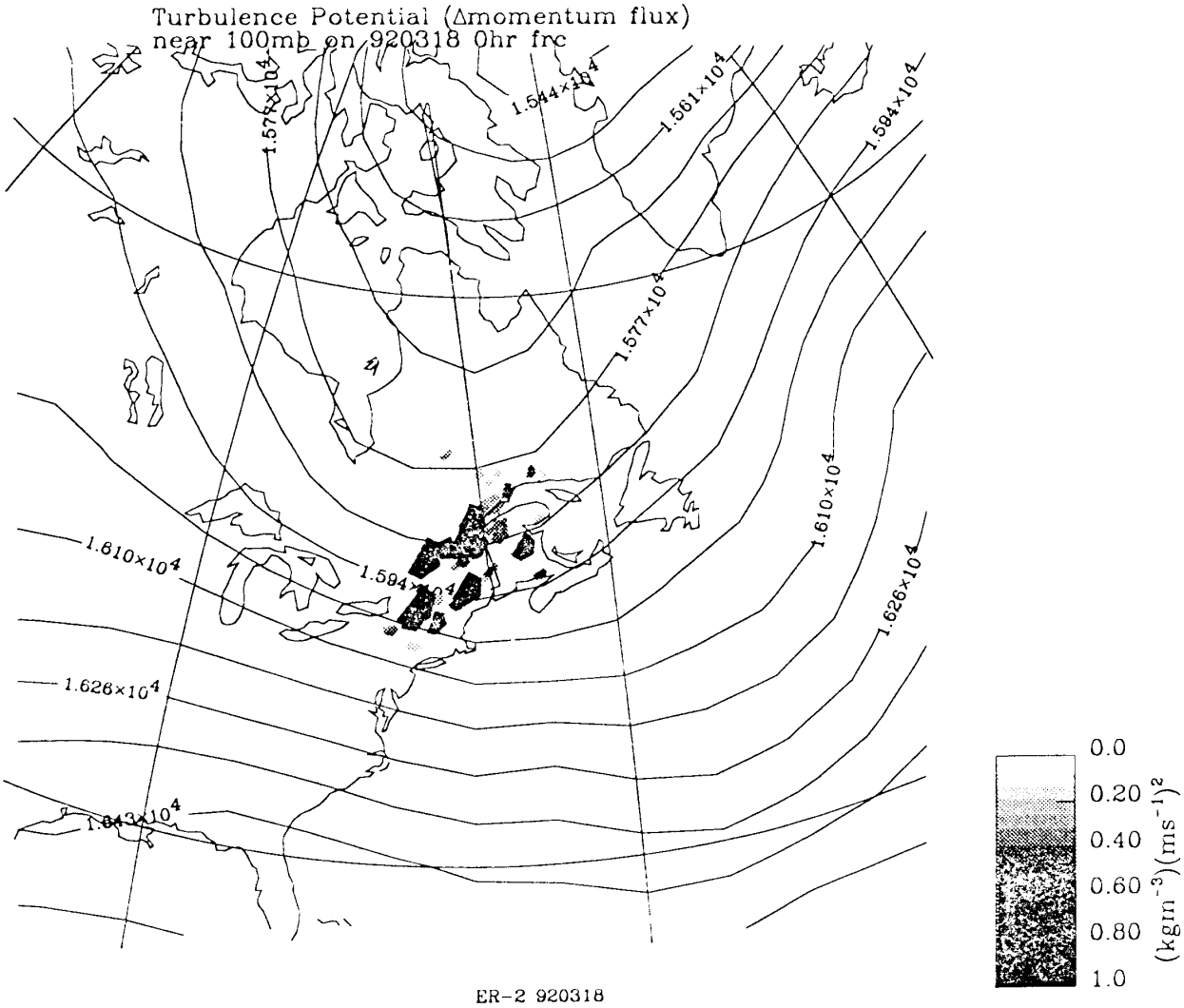
Turbulence Potential (Δmomentum flux)
near 100mb on 920318 0hr frc
1.578×10^4
1.544×10^4
1.561×10^4
1.594×10^4
1.577×10^4
1.610×10^4
1.610×10^4
1.594×10^4
1.626×10^4
1.626×10^4
1.643×10^4
0.0
0.20
0.40
0.60
0.80
1.0
(kgm^-3)(ms^-1)^2
ER-2 920318

Fig 4a

Geopotential Height 920116

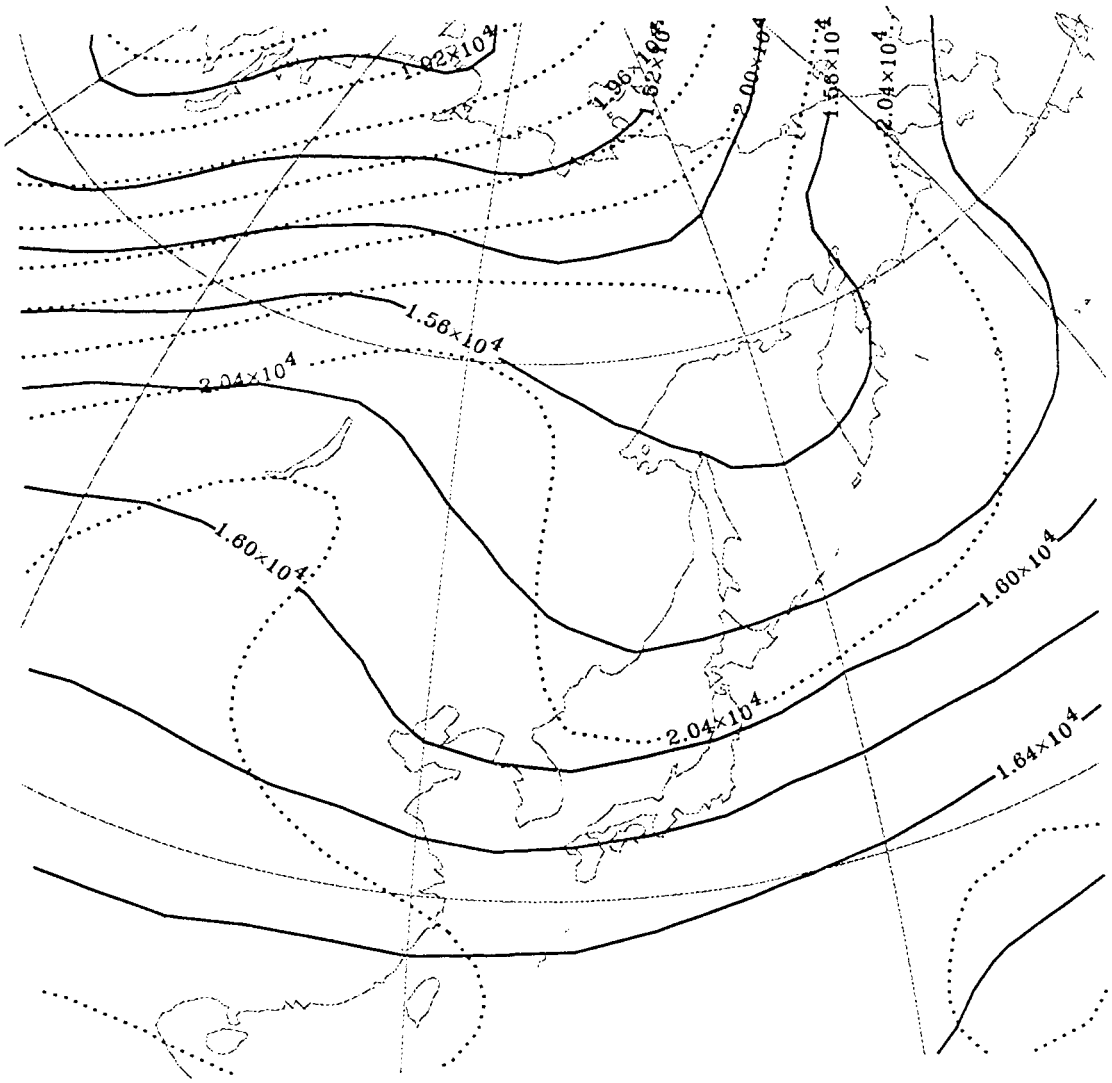

Fig. 5a